Multiscale Shape Priors for 3D Branching Structures in Vasculature Segmentation

Research report

Amelio Vazquez-Reina[1], Eric Miller[2], Sarah Frisken[3], Dr. Adel Malek[4]

✉ [1]avazqu01@cs.tufts.edu, [2]elmiller@ece.tufts.edu, [3]frisken@cs.tufts.edu
[4]amalek@tufts-nemc.org

[1,3]Department of Computer Science, Tufts University
[2] Department of Electrical and Computer Engineering, Tufts University
[4] Department of Neurosurgery, Tufts-New England Medical Center

March 3, 2008

Abstract

In this paper we present a multiscale non-parametric shape model for the segmentation of 3D branching structures such as vasculature or biological neuronal networks. The proposed technique models these structures as surfaces formed by varying-sized interconnected cylinders using higher order active contours. A geometric shape model is built using this approach and incorporated into a surface estimation problem. The model is defined as a geometric cost function that favors the formation of 3D branching shapes when minimized. The resulting functional is incorporated into an active contour framework that is evolved using level set methods. The proposed method is applied to vasculature segmentation in images obtained from 3D digital subtraction angiography. This technique is novel in that it extends previous higher order active contours models for the modeling of branching structures in 3D; it uses the geodesic metric instead of the Euclidean to define the region of interaction between boundary subsets of points; and it defines a shape model that is multiscale, which was not possible with previous higher order active contours models.

Keywords: Active contours, shape priors, level sets, vessel segmentation.

1 Introduction

The study and development of efficient methods for vasculature segmentation in 2D and 3D images is an active field of research. Vessel segmentation methods have applications in visualization, disease diagnosis and surgical planning [Hoit & Malek, 2005], [Schirmer & Malek, 2007a], [Schirmer & Malek, 2007b], [Toyota *et al.*, 2008]. Numerous algorithms have been proposed in the image processing and medical imaging literature and the vast majority depend upon the imaging modality, the application domain, the user-interaction requirements and other specific factors [Kirbas & Quek, 2004].

However, the segmentation of vessels from 3D medical images is difficult and challenging. There are several reasons for this. First, the radius of vessels varies along their longitudinal axis and depends typically on the type of vessel (e.g. smaller for thin blood vessels and larger for certain coronary arteries such as the aorta). Second, blood vessels are not isolated objects with a fixed shape; they are typically assumed to branch and bend producing a vasculature network. Third, the images obtained by the scanning devices are often noisy and show artifacts due to the non-linear nature of the imaging process. These artifacts typically make the vessels and the surrounding tissue locally difficult to recognize and separate. Finally, the segmentation of curved 3D structures presents more algorithmical difficulties than that of planar structures in 2D images [Wörz & Rohr, 2007].

The work presented in this paper tries to overcome the difficulties mentioned above in an integrated framework. We propose a level set-based active contours method that automatically extracts the vasculature from 3D angiographs. The research described in this document is mostly theoretical and serves as a Ph.D. proposal for the first author, who expects to implement the ideas presented here in the months following the publication of this report.

The rest of the paper is organized as follows. The following two subsections introduce the reader to the Aneurysm Project and 3D angiography, the imaging modality that is used to get the vasculature volume data. Section 2 looks at the related work in vessel segmentation, active contours and geometric shape priors. Section 3 shows the higher order active contours model originally introduced by [Rochery *et al.*, 2006] on which our work was based. Section 4 describes the proposed multiscale shape prior. Finally, Sections 5 and 6 discuss preliminary results and future work.

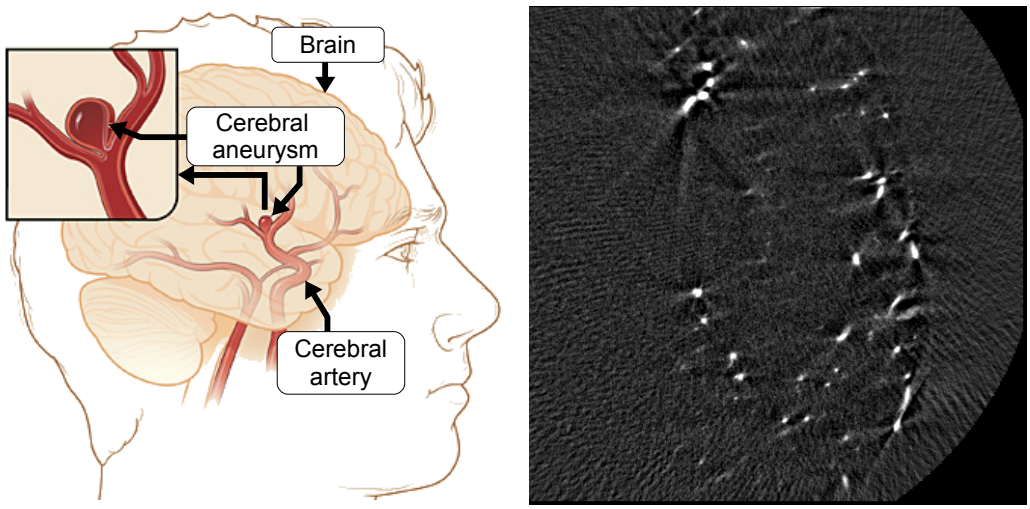

(a) (b)

Fig. 1: (a): Graphical depiction of a cerebral aneurysm[a]. (b): Cross section of a 3D-DSA image from a patient with a cerebral aneurysm.

[a] Adapted from http://www.nhlbi.nih.gov/

1.1 Motivation for research

The research presented in this paper is being conducted as part of the Aneurysm Project at Tufts University. The goal of this project is the study of techniques for vessel extraction in 3D angiographs and of algorithms for the automatic detection and classification of brain aneurysms.

Brain aneurysms are abnormal dilations in the intracranial vasculature. These dilations usually occur at the base of the brain near the Circle of Willis, the circle of arteries that supplies blood to the brain (see Figure 1(a)). Aneurysms can grow, leak, and even rupture, spilling blood into the surrounding tissue and causing what is known as a subarachnoid hemorrhage [Edlow *et al.*, 2007]. The rupture of an aneurysm can produce permanent severe damage in the nervous system or even death. According to the U.S. Department of Health and Human Services, around 30,000 people died from brain aneurysm ruptures in 2004, accounting for 1% of the total number of deaths in the same year [Heron, 2007], [Edlow *et al.*, 2007]. The factors that cause aneurysms to form and ultimately to rupture are believed to be both physiological and developmental [Lasheras, 2007]. They are phisiological,

because it has been shown that the lack of elastin and collagen is a main factor in the formation of aneuryms. Elastin and collagen are proteins that regulate the elasticity, strength and thickness of blood vessel walls. They are developmental, because it has been also shown that the geometry of an aneurysm determines its tendency to grow and rupture. Aneurysms are for example more likely to grow in certain angles between the main axis of the aneurysm and the adjacent vessel.

The goal of the Aneurysm Project is two-fold. First, to develop algorithms that efficiently extract the vasculature from 3D angiographs, an imaging modality that will be described in the following section. This is the main focus of the paper and the task on which the first author is currently working. Second, the Aneurysm Project researches the correlation between the geometry of the vasculature and the formation, growth and/or rupture of aneurysms.

1.2 The image acquisition process

The images used in the Aneurysm Project are given directly in the format of volume data by a 3D-Digital Subtraction Angiography (3D-DSA) device currently used at the Tufts-New England Medical Center[1]. 3D-DSA is an imaging modality that allows for the visualization of blood vessels in a bony or dense soft tissue environment.

The acquistion process occurs in 3D-DSA in three steps [Toyota *et al.*, 2008]. First, a catheter is guided from the femoral artery of the patient under study to the ascending aorta and positioned in the internal carotid or vertebral artery with the suspected intracranial aneurysm. Second, an X-Ray contrast agent is injected through the catheter into the targeted arterial vessel. Third, the C-arms of the 3D-DSA device generates an X-Ray field between its arms while it rotates in a continuous 200° around the patient's head placed in the isocenter. The device measures the linear attenuation of the media to the X-ray field and reconstructs the volume data once the scanning is completed. The acquisition process takes less than a minute to finish. The extracted images by the 3D-DSA device used in our experiments have a size of 256 by 256 by 229 and a spatial resolution of 0.5 mm. Figure 1(b) shows a sample slice obtained from one of our images.

[1] 3D-DSA is also known as 3D Rotational Angiography (3DRA) or as 3D Angiography (3DA).

2 Related work

The image segmentation method proposed in this paper is based on active contours. Active contours are deformable models that were originally introduced in a parametric fashion in [Kass *et al.*, 1988] as "Snakes". Nonparametric active contours (usually known as geometric active contours) were later introduced in [Caselles *et al.*, 1997] with the help of the level sets-based evolution framework introduced in [Osher & Sethian, 1988] and [Osher & Shu, 1991].

Most active contours models include cost functions (also known in the literature as energy functionals or energy terms) that either search for contours (surfaces) that move towards the boundaries of the object to be detected [Kimmel & Bruckstein, 2003], or search for contours that part the image in homogeneous regions [Chan & Vese, 2001] when minimized. The former uses edge detectors typically based on the gradient of the image to find the boundaries of the objects. The latter usually looks at the statistics of the image intensity inside and outside the closed contour.

Classical active contours based solely on image terms do not have prior information about the geometry or the shape of the objects that are being segmented. This results in a number of drawbacks. First, they are not able to distinguish between objects with similar image properties. This presents an important difficulty in the segmentation of vasculature in certain imaging modalities, such as computed tomography angiography, where the bones and the blood vessels have similar edge profiles and intensity histograms. Second, the lack of prior knowledge about the shape and geometry can produce oversegmentation and undersegmentation of the image [Xie & Mirmehdi, 2008] due to the non-convexity nature of the energy functionals used.

2.1 Learned shape priors

A number of segmentation methods have been proposed to define models that capture the shape and geometry of vasculature [Hoover *et al.*, 2000], [Tyrrell *et al.*, 2007], [Li & Yezzi, 2007], [Wörz & Rohr, 2007]. However, most of these models are usually parametric (e.g. superellipsoids, cylinders) and cannot be used in conjunction with geometric active contours driven by level sets. In addition, there has been much work in the last ten years defining and incorporating statistical shape priors that can be used in active contours driven by level sets [Chen *et al.*, 2001], [Cootes *et al.*, 1995], [Wang & Staib,

1998], [Kim *et al.*, 2007a], [Tsai *et al.*, Feb. 2003]. These methods usually add a learned prior to the energy functional that gives priority to some shapes over others. However, these priors only behave well for objects whose shape varies slightly across several samples, usually up to an affine transformation (rotation, translation, dilation, and shear) [Kim *et al.*, 2007a]. The graph topology of the human vasculature is known to change from patient to patient (e.g. different number of nodes and edges) [Aylward *et al.*, 2005]. The topology changes even more drastically if different regions of the body are considered. These variations cannot be completely modeled considering only small variations of affine transformations, and a more powerful solution is needed.

2.2 Non-learned shape priors

Some work has been done in the derivation and implementation of non-learned shape priors that model the geometry of the vasculature. [Nain *et al.*, 2004] define a "soft shape prior" that penalizes segmentation leaks (strong undersegmentation). Their shape filter fixes the percentage of points that fall both within a ball centered at each point inside the contour and the contour's enclosed region. The radius of the ball is given manually beforehand relative to the maximum vessel width. The main drawbacks of their shape prior are that it only works at a fixed scale and that it suffers from oversegmentation near branches of the vasculature, where the size of the maximally inscribed balls is slightly bigger than along a vessel. [Li & Yezzi, 2007] models the surface of blood vessels in 3D images as 4D paths given by a series of spheres along the centerline of a vessel. The surface is found as the 4D path that minimizes the length of all possile trajectories between two 4D endpoints (spheres) given by the user. The 4D space arclength is weighted by the mean and variance of the region enclosed by the surface. Their shape prior is multiscale since it can deal with vessels of varying sizes, but it does not handle branches automatically. Finally, it needs initialization from the user in the form of maximally inscribed spheres at each end point of the vessel to be segmented.

3 Higher order active contours

Higher order active contours were originally introduced by Rochery *et. al* in [Rochery *et al.*, 2006] and [Rochery *et al.*, 2007]. These new active con-

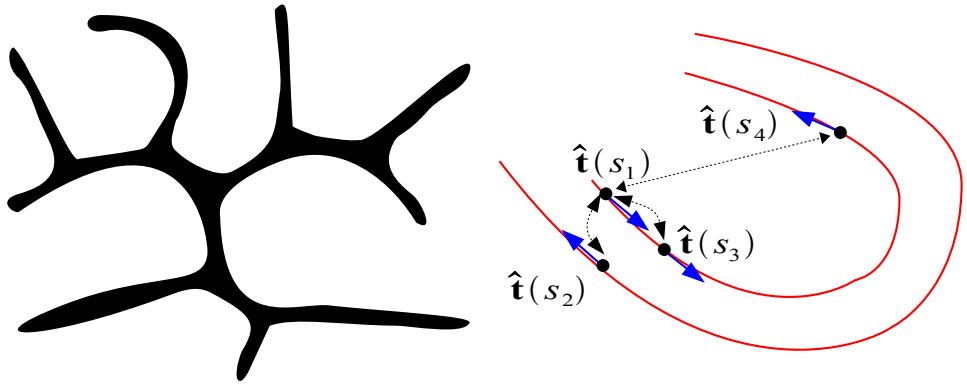

(a) (b)

Fig. 2: Shape prior introduced in [Rochery *et al.*, 2006]. (a): Example of a 2D branching structure that is favored by the energy functional of Equation 1. (b): Equation 1 forces points with parallel tangent vectors such as $\hat{\mathbf{t}}(s_1)$ and $\hat{\mathbf{t}}(s_3)$ to get closer, and points with antiparallel tangent vectors such as $\hat{\mathbf{t}}(s_1)$ and $\hat{\mathbf{t}}(s_4)$ to stay apart at a distance of at least d_{min}.

tours differ from previous models in that they can define cost functions that depend on the global geometry of the contour. The minimization of these functionals results in contour speeds that depend on the whole boundary of the contour and their interior, allowing thus for the definition of shape constrains. This differs from classical linear functionals where the contour speeds usually depend on infinitesimals defined in a neighborhood of each point of the contour, such as weighted line elements [Caselles *et al.*, 1997] or area and volume elements [Chan & Vese, 2001].

The main idea behind higher order active contours is the definition of cost functionals with multiple integrals over the boundaries and the enclosed regions[2]. This way, the new energy functionals can model non-local interactions between subsets of points in the contour boundary or between subsets of points and the image data. Rochery *et. al.* used a higher order active contour model to define quadratic energies that create a shape prior for the extraction of roads from 2D satellite imagery. To do so, they defined a objective function that when minimized it favours the segmentation of 2D shapes with a branching structure, such as the one in Figure 2(a). The original

[2] The use of multiple integrals over the same domain creates polynomial functionals of arbitrary order, and thus non-linear.

energy term is given as:

$$E_{\text{2D HOAC}} = -\iint_{\delta D} \hat{\mathbf{t}}\,(s) \cdot \hat{\mathbf{t}}\,(s')\,\psi\,(||C(s) - C(s')||)\;\, dsds' \tag{1}$$

where C is a curve (contour) that maps points from $\mathbb{R}$ to $\mathbb{R}^2$ and that tries to fit to the boundaries of the object to be segmented when the energy is minimized. The parameters s and s' define arc-length parameterizations in the domain δD of the curve C, and $\hat{\mathbf{t}}\,(s)$ and $\hat{\mathbf{t}}\,(s')$ are tangent vectors to the contour at the points $C(s)$ and $C(s')$. The term $||C(s) - C(s')||$ measures the Euclidean distance between the points $C(s)$ and $C(s')$ in the boundary of the curve, and $\hat{\mathbf{t}}\,(s) \cdot \hat{\mathbf{t}}\,(s')$ measures the alignment between the tangent vectors. The function ψ is the Heaviside function which can be approximated [Osher & Fedkiw, 2002] as

$$\psi\,(x) = \begin{cases} 2 & x < d_{\min} - \epsilon \\ 0 & x > d_{\min} + \epsilon \\ 1 - \frac{x - d_{min}}{\epsilon} - \frac{1}{\pi}\sin\left(\pi\frac{x - d_{min}}{\epsilon}\right) & \text{otherwise} \end{cases} \tag{2}$$

where d_{min} is a parameter that is set heuristically *a priori* to model the radius of the region of interaction between points on the surface.

When $\hat{\mathbf{t}}\,(s)$ and $\hat{\mathbf{t}}\,(s')$ are both parallel (collinear vectors with the same direction), the energy functional decreases if the Euclidean distance between $C(s)$ and $C(s')$ does. On the other hand, when $\hat{\mathbf{t}}\,(s)$ and $\hat{\mathbf{t}}\,(s')$ are antiparallel (collinear vectors with opposed directions), the energy increases when the points get closer than d_{min}. This idea is shown graphically in Figure 2(b).

Equation 1 works well for 2D images, where both parallel and antiparallel tangent vectors have enough information to identify the tangent space at each point on a curve. However, these concepts cannot be extended directly to 3D, since the tangent space to a surface in 3D is isomomorphic to $\mathbb{R}^2$. Another drawback of Equation 1 is that it requires that the parameter d_{min} is given *a priori*. This means that the width of the roads to be extracted should be known ahead. In vasculature segmentation that would translate into the fact that the diameter of the vessels should be also known ahead.

4 Multiscale shape prior for the segmentation of vasculaure in 3D Imagery

In this section we present our shape prior for 3D branching structures based on the model presented in the previous section. To do so, a reference frame is needed for each point on the object's surface. This frame should allow for the definition of geometric point-to-point interactions invariant to the pose of the surface inside the volume data. A natural frame to work with is the Darboux frame [Gray, 2006]. Given a surface $X : (u, v) \in \Omega \subset \mathbb{R}^2 \rightarrow \mathbb{R}^3$, the Darboux frame is defined as the $\mathbb{R}^3$ orthonormal basis $(\hat{\mathbf{e}}_\mathbf{1}(u, v), \hat{\mathbf{e}}_\mathbf{2}(u, v), \hat{\mathbf{n}}(u, v))$, where $\hat{\mathbf{n}}(u, v)$, $\hat{\mathbf{e}}_\mathbf{1}(u, v)$ and $\hat{\mathbf{e}}_\mathbf{2}(u, v)$ are the normal vector and the vector of principal directions respectively, all uniquely defined at any non-umbilical point[3] in the boundary of a continuously differentiable surface[4].

Given a point $p = X(u, v)$ on a surface like the one defined above, its normal vector can be obtained as $\hat{\mathbf{n}} = (X_u \times X_v) / (||X_u \times X_v||)$ with X_u and X_v referring to the first derivatives of X. Similarly, the vectors of principal directions at the same point are given by the eigenvectors $\hat{\mathbf{v}}_\mathbf{1}$ and $\hat{\mathbf{v}}_\mathbf{2}$ of the shape operator, which is defined in the domain Ω of the the surface X in terms of the first and second fundamental forms of X by the Weingarten Equations. The Weingarten Equations are given in matrix form for the basis (X_u, X_v) of the tangent space T_pX of the surface X at p by:

$$d\hat{\mathbf{n}}_{(X_u, X_v)} = \frac{1}{EG - F^2} \begin{pmatrix} MF - LG & NF - MG \\ LF - ME & MF - NE \end{pmatrix} \tag{3}$$

where the following definitions hold:

$$\begin{aligned} E(u, v) &= X_u \cdot X_u & L(u, v) &= \hat{\mathbf{n}} \cdot X_{uu} \\ F(u, v) &= X_u \cdot X_v & M(u, v) &= \hat{\mathbf{n}} \cdot X_{uv} \\ G(u, v) &= X_v \cdot X_v & N(u, v) &= \hat{\mathbf{n}} \cdot X_{vv} \end{aligned} \tag{4}$$

with X_{uu} X_{uv} and X_{vv} referring to the second derivatives of X. The eigen-

[3] Non-umbilical points are points where the surface is not locally spherical. That is, points where the principal curvatures are not identical.

[4] For practical reasons it will be assumed in the rest of the paper that the surfaces under consideration are at least of class G^3.

vectors $(\hat{\mathbf{v}}_\mathbf{1}, \hat{\mathbf{v}}_\mathbf{2})$ of the shape operator $d\hat{\mathbf{n}}_{(X_u, X_v)}$ are given by:

$$\begin{aligned}
&\hat{\mathbf{v}}_\mathbf{1}(u,v) = \\
&\left\{ \frac{-GL + NE + \sqrt{-4\left(M^2 - LN\right)\left(F^2 - GE\right) + \left(GL - 2FM + NE\right)^2}}{2FL - 2ME}, 1 \right\} \\
&\hat{\mathbf{v}}_\mathbf{2}(u,v) = \\
&\left\{ -\frac{GL - NR + \sqrt{-4\left(M^2 - LN\right)\left(F^2 - GR\right) + \left(GL - 2FM + NR\right)^2}}{2FL - 2MR}, 1 \right\}
\end{aligned} \tag{5}$$

The principal directions of the surface X are thus given by $\hat{\mathbf{e}}_\mathbf{1} = v_{11}X_u + v_{12}X_v$ and $\hat{\mathbf{e}}_\mathbf{2} = v_{21}X_u + v_{22}X_v$ with $\hat{\mathbf{v}}_\mathbf{1} \equiv (v_{11}, v_{12})$ and $\hat{\mathbf{v}}_\mathbf{2} \equiv (v_{21}, v_{22})$.

Each of the eigenvectors of $d\hat{\mathbf{n}}_{(u,v)}$ has an associated eigenvalue k_1, k_2 which corresponds to either the maximum or minimum normal curvatures k_{max} and k_{min} of the surface at the point $p = X(u,v)$:

$$\begin{aligned}
&k_1(u,v) = \\
&\frac{GL - 2FM + NR - \sqrt{-4\left(M^2 - LN\right)\left(F^2 - GR\right) + \left(GL - 2FM + NR\right)^2}}{2\left(F^2 - GR\right)} \\
&k_2(u,v) = \\
&\frac{GL - 2FM + NR + \sqrt{-4\left(M^2 - LN\right)\left(F^2 - GR\right) + \left(GL - 2FM + NR\right)^2}}{2\left(F^2 - GR\right)}
\end{aligned} \tag{6}$$

The Darboux frame defined above can be used to define point-to-point relationships that capture the local geometry of the vasculature. We first make the assumption that the surface formed by the boundary of the vasculature can be represented as a series of interconnected perfect local cylinders. This assumption has been shown to be reasonable previously [Wörz & Rohr, 2007], [Makowski *et al.*, 2006], and in any case, the errors derived from the inaccuracy of this assumption will still be balanced with the combination of image-terms (see section 2 above).

In order to build the desired shape prior we will use the following fact: Given a point p on a cylinder $C : (u,v) \rightarrow \mathbb{R}^3$ and its Darboux frame $(\hat{\mathbf{e}}_\mathbf{1}(u,v), \hat{\mathbf{e}}_\mathbf{2}(u,v), \hat{\mathbf{n}}(u,v))$ it is possible to estimate the Darboux frame

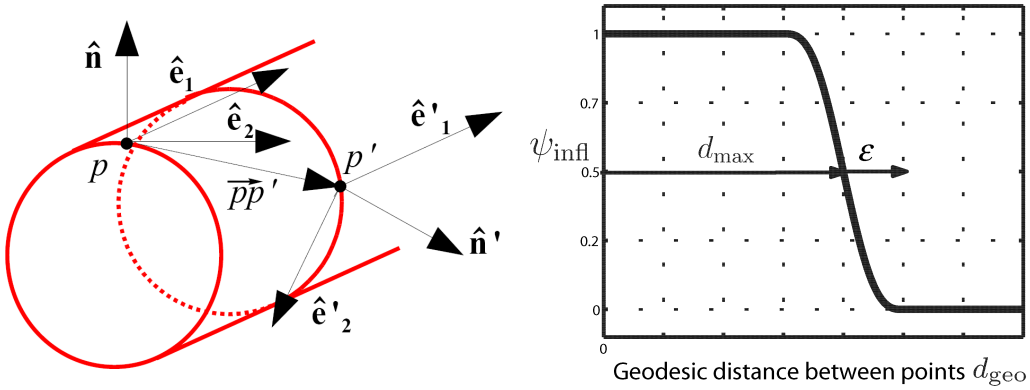

(a) (b)

Fig. 3: (a): Estimation of Darboux frames on a cylinder following the notation from Equation 7. (b): The Heaviside function ψ_{infl} defined in Equation 17.

$(\hat{\mathbf{e}}_1(u',v'), \hat{\mathbf{e}}_2(u',v'), \hat{\mathbf{n}}(u',v'))$ and its location relative to the former at any point p' on the same cylinder given a unit direction vector between them $\hat{pp'}$. Figure 3(a) shows this idea graphically.

We define with some abuse of notation the following Darboux frames:

$$\begin{aligned}(\hat{\mathbf{e}}_1, \hat{\mathbf{e}}_2, \hat{\mathbf{n}}) &= (\hat{\mathbf{e}}_1(u,v), \hat{\mathbf{e}}_2(u,v), \hat{\mathbf{n}}(u,v)) \text{ at } p = X(u,v) \\ (\hat{\mathbf{e}}'_1, \hat{\mathbf{e}}'_2, \hat{\mathbf{n}}') &= (\hat{\mathbf{e}}_1(u',v'), \hat{\mathbf{e}}_2(u',v'), \hat{\mathbf{n}}(u',v')) \text{ at } p' = X(u',v')\end{aligned} \tag{7}$$

We assume without lost generality that the principal directions $\hat{\mathbf{e}}_1$, $\hat{\mathbf{e}}'_1$ correspond to the eigenvalues k_{min} and k'_{min} and $\hat{\mathbf{e}}_2$ and $\hat{\mathbf{e}}'_2$ to the eigenvalues k_{max} and k'_{max}, all at the points p and p' respectively. We then state the following:

1. The Darboux frame $(\hat{\mathbf{e}}'_1, \hat{\mathbf{e}}'_2, \hat{\mathbf{n}}')$ can be estimated to be located at an Euclidean distance $\tilde{d}_p$ from p such that:

$$\tilde{d}_p(u,v,u',v') = 2\frac{1}{k_{max}} \cdot \sqrt{\frac{1-\left(\hat{pp'} \cdot \hat{\mathbf{e}}_2\right)^2}{1-\left(\hat{pp'} \cdot \hat{\mathbf{e}}_1\right)^2}} \tag{8}$$

The function $\tilde{d}_{p'}(u,v,u',v')$ can be defined similarly for p'[5].

[5] A more detailed explanation of the derivation of this estimated Euclidean distance

2. The triplet $\left(\widetilde{\hat{\mathbf{n}}}', \widetilde{\hat{\mathbf{e}}}'_{\mathbf{1}}, \widetilde{\hat{\mathbf{e}}}'_{\mathbf{2}}\right)$, defined as the estimate of $(\hat{\mathbf{n}}', \hat{\mathbf{e}}'_{\mathbf{1}}, \hat{\mathbf{e}}'_{\mathbf{2}})$, is related to $(\hat{\mathbf{n}}, \hat{\mathbf{e}}_{\mathbf{1}}, \hat{\mathbf{e}}_{\mathbf{2}})$ through the following equation:

$$\begin{aligned} \widetilde{\hat{\mathbf{n}}}'(u, v, u', v') &= \mathrm{Rot}\left(\hat{\mathbf{n}}\right)_{(\hat{\mathbf{e}}_{\mathbf{1}}, \alpha_p)} \\ \widetilde{\hat{\mathbf{e}}}'_{\mathbf{1}}(u, v) &= \hat{\mathbf{e}}_{\mathbf{1}} \\ \widetilde{\hat{\mathbf{e}}}'_{\mathbf{2}}(u, v, u', v') &= \mathrm{Rot}\left(\hat{\mathbf{e}}_{\mathbf{2}}\right)_{(\hat{\mathbf{e}}_{\mathbf{1}}, \alpha_p)} \end{aligned} \tag{9}$$

where the notation $\mathrm{Rot}\left(\hat{\mathbf{a}}\right)_{\left(\hat{\mathbf{b}}, \alpha\right)}$ refers to the rotation of a vector $\hat{\mathbf{a}}$ around a vector $\hat{\mathbf{b}}$ of an angle of α.

The angle α_p can be obtained from

$$\alpha_p(u, v, u', v') = 2 \arccos\left(\hat{\mathbf{n}} \cdot \hat{p\hat{p}'}_{2D}\right) \tag{10}$$

where $\hat{p\hat{p}'}_{2D}$ is the projection of the vector $\hat{p\hat{p}'}$ onto the 3D plane spanned by the vectors $\hat{\mathbf{n}}$ and $\hat{\mathbf{e}}_2$.

Similar expressions can be obtained for the estimates from p'.

Using the above estimates, we can measure the fitting of the infinitesimal neighborhoods of p and p' to a perfect cylinder. In a perfect cylinder, the estimated frames at p and p' given by Equation 9 and the true Darboux frames should coincide. The alignment between them can be measured with the help of a function ψ_{alig} defined as:

$$\psi_{\mathrm{alig}}(u, v, u'v') = \psi_{\mathrm{alig}_p} \psi_{\mathrm{alig}_{p'}} \tag{11}$$

with

$$\begin{aligned} \psi_{\mathrm{alig}_p}(u, v, u'v') &= \frac{1}{2}\left(\left(\frac{\hat{\mathbf{n}} \cdot \widetilde{\hat{\mathbf{n}}} + \hat{\mathbf{e}}_{\mathbf{1}} \cdot \widetilde{\hat{\mathbf{e}}}_{\mathbf{1}} + \hat{\mathbf{e}}_{\mathbf{2}} \cdot \widetilde{\hat{\mathbf{e}}}_{\mathbf{2}}}{3}\right) + 1\right) \\ \psi_{\mathrm{alig}_{p'}}(u, v, u'v') &= \frac{1}{2}\left(\left(\frac{\hat{\mathbf{n}}' \cdot \widetilde{\hat{\mathbf{n}}}' + \hat{\mathbf{e}}'_{\mathbf{1}} \cdot \widetilde{\hat{\mathbf{e}}}'_{\mathbf{1}} + \hat{\mathbf{e}}'_{\mathbf{2}} \cdot \widetilde{\hat{\mathbf{e}}}'_{\mathbf{2}}}{3}\right) + 1\right) \end{aligned} \tag{12}$$

where ψ_{alig} increases when the estimated frames at p and p' get closer to the true Darboux frames. The dot products used in Equation 12 measure

will be provided in the annex in future reports.

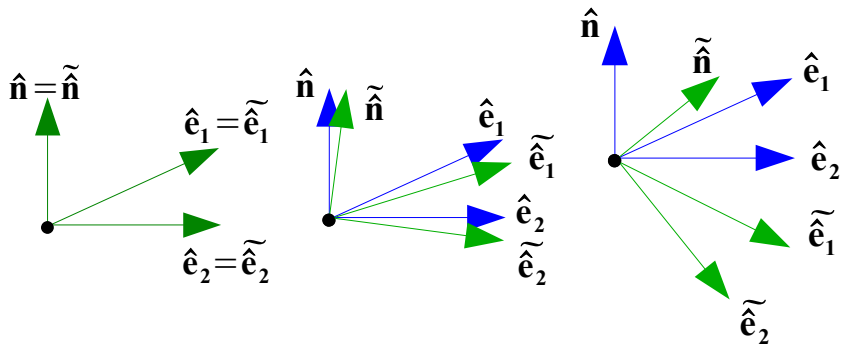

(a) (b) (c)

Fig. 4: Alignment between frames $\left(\tilde{\hat{\mathbf{e}}}_1, \tilde{\hat{\mathbf{e}}}_2, \tilde{\hat{\mathbf{n}}}\right)$ and $(\hat{\mathbf{e}}_1, \hat{\mathbf{e}}_2, \hat{\mathbf{n}})$. (a): Perfect alignment (ψ_{alig_p}=1). (b): High alignment ($\psi_{\text{alig}_p} \approx 1$). (c): Medium alignment ($0 < \psi_{\text{alig}_p} < 1$).

the alignment betweeen a vector in one of the estimated frames and the same vector in the corresponding true Darboux frame. The constants in Equation 12 were set so that ψ_{alig}, ψ_{alig_p} and $\psi_{\text{alig}_{p'}}$ take values in the range $[0, 1]$. Higher values of ψ_{alig} mean better fitness of the infinitesimals neighborhoods of p and p' to a cylindrical shape. Figure 4 shows graphically this idea with several examples where the alignment between $\left(\tilde{\hat{\mathbf{e}}}_1, \tilde{\hat{\mathbf{e}}}_2, \tilde{\hat{\mathbf{n}}}\right)$ and $(\hat{\mathbf{e}}_1, \hat{\mathbf{e}}_2, \hat{\mathbf{n}})$ is measured[6].

Similarly, the accuracy of the estimates for the Euclidean distance between the Darboux frames at p and p' can be measured with the help of a function ψ_{dist} defined as:

$$\psi_{\text{dist}}\left(u, v, u'v'\right) = \frac{1}{|\tilde{d}_p - d|} \frac{1}{|\tilde{d}_{p'} - d|} \tag{13}$$

where d is the true Euclidean distance between the points $p = X\left(u, v\right)$ and p' $= X\left(u', v'\right)$; and $\tilde{d}_{p'}$ is the estimated Euclidean distance defined in Equation 8. The function ψ_{dist} takes values between zero and infinite and increases when the estimates are accurate ($\tilde{d}_p \approx d$, $\tilde{d}_{p'} \approx d$), and decreases when they are not.

[6] Similar examples could be given for the alignment between $\left(\tilde{\hat{\mathbf{e}}}'_1, \tilde{\hat{\mathbf{e}}}'_2, \tilde{\hat{\mathbf{n}}}'\right)$ and $(\hat{\mathbf{e}}'_1, \hat{\mathbf{e}}'_2, \hat{\mathbf{n}}')$.

Finally we define the function ψ_{joint} which will be refered as the "joint-cylindricity" and measures how the infinitesimal neighborhoods of p and p' fit to a unique perfect cylinder based on the previous measurements:

$$\psi_{\text{joint}}\left(u, v, u'v'\right) = \psi_{\text{alig}} \cdot \psi_{\text{dist}} \tag{14}$$

where ψ_{joint} takes values between zero and infinite and is monotonically increasing as the surface neighborhoods of p and p' fit to some cylinder.

We now define an energy functional E_{entire} that evaluates the cilindricity of the surface X as follows:

$$E_{\text{entire}}\left(X\right) = -\iiiint_{\delta D} \psi_{\text{joint}}\left(u, v, u'v'\right)\ dudvdu'dv' \tag{15}$$

where δD now refers to the domain of the surface X. The functional E_{entire} measures the fitting of the entire surface X to a perfect cylinder. From this point we can proceed to measure the cylindricity of the surface *locally*. The idea is to measure how easily the surface could be sliced in perfect small cylinders of varying size. For this reason we define a new function ψ_{infl} that will help constrain the evaluation of the joint-cylindricity to a local neighborhood around each point. This will define a constrained region of mutual interaction between pairs of points in the surface that can be bounded in a geodesic-sense as follows:

$$E_{\text{sliced}}\left(X\right) = -\iiiint_{\delta D} \psi^{k}_{\text{joint}}\left(u, v, u'v'\right) \psi^{j}_{\text{infl}}\left(u, v, u'v'\right)\ dudvdu'dv' \tag{16}$$

where the parameters j and k are scalar values that can be defined heuristically to balance the influence between ψ_{joint} and ψ_{infl} in the functional E_{sliced}. ψ_{infl} is a Heaviside function that can be approximated as:

$$\psi_{\text{infl}}\left(u, v, u', v'\right) = \begin{cases} 1 & d_{\text{geo}} < d_{\max} - \epsilon \\ 0 & d_{\text{geo}} > d_{\max} + \epsilon \\ \frac{1}{2}\left(1 - \frac{d_{\text{geo}} - d_{max}}{\epsilon} - \frac{1}{\pi}\sin\left(\pi\frac{d_{\text{geo}} - d_{max}}{\epsilon}\right)\right) & \text{otherwise} \end{cases} \tag{17}$$

where the following parameters are defined:

- $d_{\max}$: A function that gives the maximum length of the local cylinder as a function of the average of the radii of the cylinders that best fit

the neighborhoods of $X(u,v)$ and $X(u',v')$ respectively. It is defined as:

$$d_{\max}(u,v) = K_1 \frac{1}{2}\left(\frac{1}{k_{\max}} + \frac{1}{k'_{\max}}\right) \tag{18}$$

with K_1 a parameter given *a priori* that can be determined heuristically. The quotient $1/k_{\max}$ is the radius of the cylinder that best fits the infinitesimal neighborhood of point $X(u,v)$. Similarly, $1/k'_{\max}$ is the radius of the cylinder that best fits the infinitesimal neighborhood of point $X(u',v')$. $d_{\max}$ is thus the function that enables for a multiscale shape prior. The length of the local cylinders can be typically chosen to be twice as big as their radii (i.e. $K_1 \approx 2$).

- d_{geo}: The geodesic riemannian distance between the points $p = X(u,v)$ and $p' = X(u',v')$ on the surface X defined by:

$$d_{\text{geo}}(u,v,u',v') = \inf \int_0^1 ||C'(t)||\ dt \tag{19}$$

where $C(t) : \mathbb{R} \to \mathbb{R}^2$ is a smooth simple curve with $t \in [0,1]$, $C(0) = X(u,v)$, $C(1) = X(u',v')$, $C'(t) \in TX$, with TX the tangent space of the surface X.

- ϵ: A strictly positive parameter defined as $\epsilon = K_2 d_{\max}$ that controls the approximation of the Heaviside function ψ_{infl}. K_2 is determined heuristically. Values for K_2 of 0.01 are typically considered [Rochery, 2005].

4.1 Combination with other segmentation terms

As was mentioned in section 2, the shape prior defined in Equation 16 needs to be combined with image terms so that it can segment the volume data. Similarly, we can train the segmentation process with several samples through the use of learned shape priors such as the ones introduced in [Kim *et al.*, 2007a] or those discussed in Subsection 2.1. Grouping the image terms in E_{img} and the learned shape priors in E_{LSP}, we can define an energy functional E_{total} that integrates the different functional terms:

$$E_{\text{total}} = K_{\text{img}} E_{\text{img}} + K_{\text{LSP}} E_{\text{LSP}} + K_{\text{sliced}} E_{\text{sliced}} \tag{20}$$

where the regularization parameters K_{img}, K_{LSP} and K_{sliced} can be chosen heuristically. The minimization of E_{total} would yield the surface that extracts the vasculature.

4.2 Energy minimization

Finding the surface that separates the vasculature from the background for each image according to our model is equivalent to finding the surface that minimizes the functional of Equation 20. Since this problem cannot be generally solved analytically (statically) [Osher & Paragios, 2003], the minima is found iteratively with the method of gradient descent. This way, the system is initialized with initial conditions $X = X_0$, and the gradient descent equation yields the following Euler-Lagrange Equation:

$$\frac{\delta X}{\delta t} = -\frac{\delta E_{\text{total}}}{\delta X\,(u,v)} \tag{21}$$

The derivation of the gradient descent equations for the terms E_{img} and E_{LSP} can be found in the literature [Kimmel & Bruckstein, 2003], [Chan & Vese, 2001], [Kim *et al.*, 2007b]. We thus focus here on the derivation of $\delta E_{\text{sliced}}/\delta X\,(u,v)$, also known as the Gâteaux derivative of the functional E_{sliced}. The Gâteaux derivative can be obtained from the computation of the Gâteaux differential δE_{sliced} using the inner product defined for the Hilbert space L^2 as follows:

$$\delta E_{\text{sliced}} = \langle \frac{\delta E_{\text{sliced}}}{\delta X\,(u,v)}, \delta X\,(u,v) \rangle = \iint_{\delta D} \frac{\delta E_{\text{sliced}}}{\delta X\,(u,v)} \cdot \delta X\,(u,v)\ dudv \tag{22}$$

Similarly, the differential δE_{sliced} is defined as the linear component of an infinitesimal change ΔE_{sliced} for a perturbation ΔX of the surface X[7]:

$$\begin{aligned} \Delta E_{\text{sliced}} &= -\iiiint_{\delta D} \delta G\,(u,v,u',v')\ dudvdu'dv' + o(||\Delta X||) \\ \delta E_{\text{sliced}} &= -\iiiint_{\delta D} \delta G\,(u,v,u',v')\ dudvdu'dv' \end{aligned} \tag{23}$$

[7] It should be noted that X, the surface that represents the model, is the independent variable and therefore $\Delta X = \delta X$.

where we have that G is $\psi^k_{\text{joint}}(u,v,u'v')\,\psi^j_{\text{infl}}(u,v,u'v')$ from Equation 16. The differential of G is given by the following multivariate Taylor series:

$$\begin{aligned}\delta G =& G_{X(u,v)} \cdot \delta X(u,v) + G_{X(u',v')} \cdot \delta X(u',v') + G_{X_u(u,v)} \cdot \delta X_u(u,v) + \\ & G_{X_u(u',v')} \cdot \delta X_u(u',v') + G_{X_v(u,v)} \cdot \delta X_v(u,v) + G_{X_v(u',v')} \cdot \delta X_v(u',v') + \\ & G_{X_{uv}(u,v)} \cdot \delta X_{uv}(u,v) + G_{X_{uv}(u',v')} \cdot \delta X_{uv}(u',v') + G_{X_{uu}(u,v)} \cdot \delta X_{uu}(u,v) + \\ & G_{X_{uu}(u',v')} \cdot \delta X_{uu}(u',v') + G_{X_{vv}(u,v)} \cdot \delta X_{vv}(u,v) + G_{X_{vv}(u',v')} \cdot \delta X_{vv}(u',v')\end{aligned} \tag{24}$$

where the notation G_a means the derivative of G with respect to a. Finally, Equation 22 can be obtained from combining Equations 23 and 24 and integrating by parts.

The evolution of the surface X is done using level sets. The surface is implicitly embedded in a 4D scalar field ϕ as its zero level set. The Level Set Equation takes the following form for our problem [Osher & Paragios, 2003]:

$$\frac{\delta\phi}{\delta t} = -\nabla\phi \cdot \hat{\mathbf{n}} F = -\nabla\phi \cdot \frac{\nabla\phi}{|\nabla\phi|} F = -|\nabla\phi| F \tag{25}$$

where F is the speed of the surface in its normal direction $\hat{\mathbf{n}}$. A common option for ϕ is the distance field of X since that translates into $|\nabla\phi| = 1$. The function F is all it is needed to run the level sets evolution and it is given by the following equation[8]:

$$F = -\frac{\delta E_{\text{total}}}{\delta X(u,v)} \cdot \hat{\mathbf{n}} \tag{26}$$

5 Results

The main author of the paper has already successfully tested the image term E_{img} introduced in [Caselles *et al.*, 1997] on some of our datasets using Matlab and ITK[9]. The same author is currently working on the Gâteaux differential of the functional G (Equation 24) and will be implementing the geometric

[8] We only need the speed that is normal to the surface. The tangent component reduces to a diffeomorphism of the surface [Kimmel, 2003].

[9] ITK is an open-source library for image segmentation and registration. It can be obtained from `http://www.itk.org/`

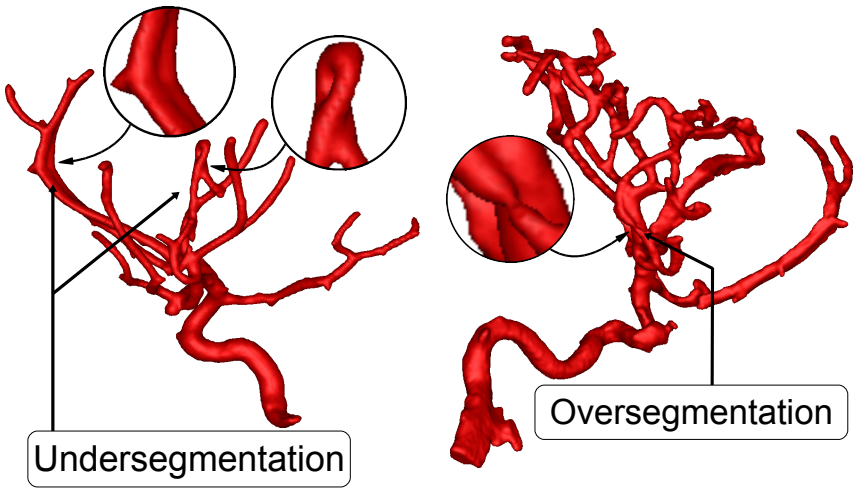

(a) (b)

Fig. 5: Some of the common problems with classical active contours models that our shape prior can help overcome. The figure shows segmentation results for four datasets obtained with the energy functional introduced in [Caselles *et al.*, 1997]. (a): The active contour ended up connecting adjacent vessels due to their proximity. (b) The active contour failed to extract a vessel with the right diameter.

shape priors introduced here using ITK during his summer intership at The Connectome Project[10].

Figures 5 and 6 show the segmentation results for 3D angiographs of the brain vasculature of some of our patients. These results were obtained for values K_{LSP}=0 and K_{sliced}=0 in Equation 26. The image term E_{img} used in this test is the one introduced in [Caselles *et al.*, 1997].

Figures 5(a) and 5(b) show oversegmentation and undersegmentation problems in regions where the image information is ambiguous. In Figure 5(a), the image term ended up connecting adjacent vessels due to their spatial proximity and similar intensity profiles. In Figure 5(b), the segmentation failed to extract the boundary of one of the vessels with the right diameter. The shape prior presented in this paper could help avoid both of these

[10] The Connectome Project is a research project at the research center of Initiative in Innovative Computing at Harvard University: http://iic.harvard.edu/projects/connectome.html

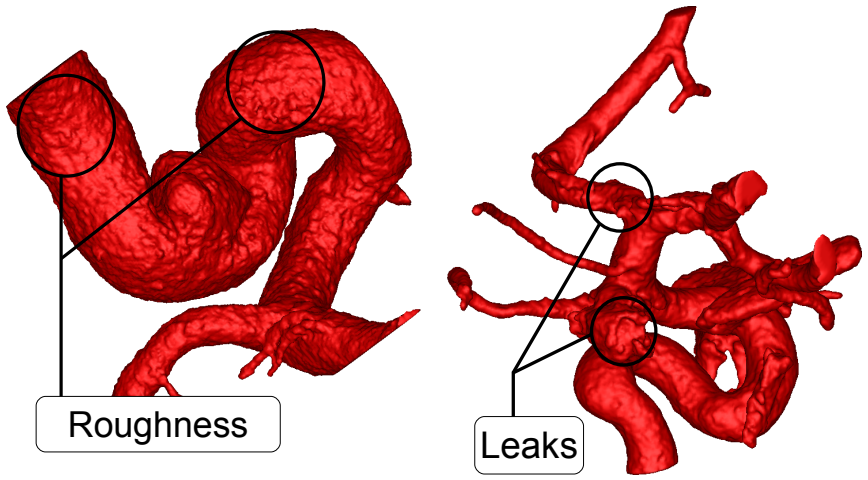

(a) (b)

Fig. 6: Some of the common problems with classical active contours models that our shape prior can help overcome. The figure shows segmentation results for four datasets obtained with the energy functional introduced in [Caselles *et al.*, 1997]. (a) Classical first and second derivatives-based smoothing cannot yield smooth boundaries at multiple scales. (b): Ambiguous image information and blurry edges produce leaking if only image-based functionals are used to drive the active contours.

problems by constraining the evolution to force local cylindricity in the exctracted surface. Figure 6(a) shows a close-up of an aneurysm. The surface shows some roughness which cannot be alleviated at all scales solely with the use of classic first and/or second-derivatives-based smoothing terms in the functional. The shape prior we present here could alleviate this problem since smoother surfaces should yield an overall better alignment of Darboux frames, which is enforced by our mutiscale functional. Finally, Figure 6(b) shows a pronounced undersegmentation effect due to leaks in the evolution process in areas where the image information is ambiguous. The use of our shape prior would penalize those leaks and constrain the evolution to only generate cylindrical surfaces.

6 Other applications and future work

The current shape prior can also be applied to the detection of aneurysms. Aneurysms can be interpreted as a random surface deviation from the cylindrical geometry of healthy vasculature. The "joint-cylindricity" measure of Equation 14 should yield higher values of energy for the local neighborhoods around an aneurysm. No evolution equation is needed for this process. We expect to test this idea soon.

A problem with the current model is that the prior penalizes deviations from straight cylindrical shapes within a local neighborhood. The current shape prior can be extended to work on plastic cylindric models that offer no resistance to certain deformations. We are considering giving some plasticity to the "joint-cylindricity" term of Equation 14. This would let the local cylinders bend with no energy penalization. We would ideally like to keep the cross section of the surface rigid while allowing deformations along the longitudinal axis. These deformations would map to iso-contours of the energy functional. We are looking into low-order elasticity equations for rods using Darboux frames such as those introduced in [Ignat *et al.*, 2000]. The addition of plasticity would hopefully relax the evolution of the surface so that it better adapts to the natural geometry of the vasculature.

Another drawback of the current shape prior is the modeling of junctions and branches. In its present form, the shape prior penalizes junctions when they do not have a cylindrical appearance. We believe that this restriction could be alleviated by letting the cross sections to be also elliptical. These unaccuracies are currently compensated in the literature with learned shape priors and the image terms, but we expect to be able to model this geometrically.

Finally, we are considering the use of phase fields as implicit 4D scalar fields ϕ in which the surfaces are embedded. Phase fields have several advantages over distance fields when combined with higher order active contours [Rochery *et al.*, 2005], [Horvath & Jermyn, 2007]. The gradient descent of functionals embedded inside a phase field requires no initialization or reinitialization; and there is no need for boundary extraction nor velocity extension beyond the boundary during the minimization process.

7 Acknowledgements

The 3D images used by the team of the Aneurysm Project were courteously provided by the Department of Neurosurgery at the Tufts-New England Medical Center in Boston, MA. We would like to thank them for providing access to the imagery.

References

Aylward, Stephen R., Jomier, Julien, Vivert, Christelle, LeDigarcher, Vincent, & Bullitt, Elizabeth. 2005. Spatial Graphs for Intra-cranial Vascular Network Characterization, Generation, and Discrimination. *Pages 59–66 of: MICCAI*.

Caselles, Vicent, Kimmel, Ron, & Sapiro, Guillermo. 1997. Geodesic Active Contours. *International Journal of Computer Vision*, **22**(1), 61–79.

Chan, T. F., & Vese, L. A. 2001. Active contours without edges. *Image Processing, IEEE Transactions on*, **10**(2), 266–277.

Chen, Yunmei, Thiruvenkadam, Sheshadri, Huang, Feng, Wilson, David, Geiser, Edward A., Md, & Tagare, Hemant D. 2001. On the Incorporation of shape priors into geometric active contours. *Page 145 of: VLSM '01: Proceedings of the IEEE Workshop on Variational and Level Set Methods (VLSM'01)*. Washington, DC, USA: IEEE Computer Society.

Cootes, T. F., Taylor, C. J., Cooper, D. H., & Graham, J. 1995. Active shape models - Their training and application. *Comput. Vis. Image Underst.*, **61**(1), 38–59.

Edlow, J. A., Malek, A. M., & Ogilvy, C. S. 2007. Aneurysmal Subarachnoid Hemorrhage: Update for Emergency Physicians. *Journal of Emergency Medicine*. Article in Press.

Gray, Alfred. 2006. *Modern Differential Geometry of Curves and Surfaces with Mathematica*. Boca Raton, FL, USA: CRC Press, Inc.

Heron, Melonie. 2007. Deaths: Leading Causes for 2004. *National Vital Statistics Report*, **56**(5), 1–96.

Hoit, D. A., & Malek, A. M. 2005. Three-dimensional rotational angiographic detection of in-stent stenosis in wide-necked aneurysms treated with a self-expanding intracranial stent. *Neurosurgery*, **57**(6), 1228–1235.

Hoover, Adam, Kouznetsova, Valentina, & Goldbaum, Michael H. 2000. Locating Blood Vessels in Retinal Images by Piece-wise Threshold Probing of a Matched Filter Response. *IEEE Trans. Med. Imaging*, **19**(3), 203–210.

Horvath, P., & Jermyn, I. H. 2007 (September). A 'Gas of Circles' Phase Field Model and its Application to Tree Crown Extraction. *In: Proc. European Signal Processing Conference (EUSIPCO)*.

Ignat, A., Sprekels, J., & Tiba, D. 2000. A model of a general elastic curved rod. *Mathematical Methods in the Applied Sciences*.

Kass, M., Witkin, A., & Terzopoulos, D. 1988. Snakes: Active Contour Models. *International Journal of Computer Vision*, **1**(4), 321–331.

Kim, Junmo, Çetin, Müjdat, & Willsky, Alan S. 2007a. Nonparametric shape priors for active contour-based image segmentation. *Signal Process.*, **87**(12), 3021–3044.

Kim, Junmo, Çetin, Müjdat, & Willsky, Alan S. 2007b. Nonparametric shape priors for active contour-based image segmentation. *Signal Process.*, **87**(12), 3021–3044.

Kimmel, R., & Bruckstein, A. M. 2003. Regularized Laplacian Zero Crossings as Optimal Edge Integrators. *Int. J. Comput. Vision*, **53**(3), 225–243.

Kimmel, Ron. 2003. *Numerical Geometry of Images: Theory, Algorithms, and Applications*. SpringerVerlag.

Kirbas, C., & Quek, F. 2004. A review of vessel extraction techniques and algorithms. *ACM Computing Surveys*, **36**(2), 81–121. Cited By (since 1996): 59.

Lasheras, Juan C. 2007. The Biomechanics of Arterial Aneurysms. *Annual Review of Fluid Mechanics*, **39**(1), 293–319.

Li, H., & Yezzi, A. 2007. Vessels as 4-D Curves: Global Minimal 4-D Paths to Extract 3-D Tubular Surfaces and Centerlines. *Medical Imaging, IEEE Transactions on*, **26**(9), 1213–1223.

Makowski, P., de Koning, Patrick J. H., Angeli, Emmanuelle, Westenberg, Jos J. M., van der Geest, Rob J., & Reiber, Johan H. C. 2006. 3D Cylindrical B-Spline Segmentation of Carotid Arteries from MRI Images. *Pages 188–196 of:* Harders, Matthias, & Szkely, Gbor (eds), *ISBMS*. Lecture Notes in Computer Science, vol. 4072. Springer.

McInerney, Tim, & Terzopoulos, Demetri. 2000. Topology Adaptive Deformable Surfaces for Medical Image Volume Segmentation. *IEEE Trans. Med. Imaging*, **18**(10), 840–850.

Nain, Delphine, Yezzi, Anthony J., & Turk, Greg. 2004. Vessel Segmentation Using a Shape Driven Flow. *Pages 51–59 of: MICCAI (1)*.

Osher, Stanley, & Paragios, Nikos. 2003. *Geometric Level Set Methods in Imaging,Vision,and Graphics*. Secaucus, NJ, USA: Springer-Verlag New York, Inc.

Osher, Stanley, & Sethian, James A. 1988. Fronts Propagating with Curvature-Dependent Speed: Algorithms Based on Hamilton-Jacobi Formulations. *Journal of Computational Physics*, **79**, 12–49.

Osher, Stanley, & Shu, Chi-Wang. 1991. High-order essentially nonsocillatory schemes for Hamilton-Jacobi equations. *SIAM J. Numer. Anal.*, **28**(4), 907–922.

Osher, Stanley J., & Fedkiw, Ronald P. 2002. *Level Set Methods and Dynamic Implicit Surfaces*. Springer.

Rochery, M. 2005. *Contours actifs d'ordre suprieur et leur application la dtection de liniques dans des images de tldtection*. Ph.D. thesis, Universite de Nice Sophia Antipolis, Sophia Antipolis.

Rochery, M., Jermyn, I. H., & Zerubia, J. 2005 (October). Phase field models and higher-order active contours. *In: Proc. IEEE International Conference on Computer Vision (ICCV)*.

Rochery, Marie, Jermyn, Ian H., & Zerubia, Josiane. 2006. Higher Order Active Contours. *Int. J. Comput. Vision*, **69**(1), 27–42.

Rochery, Marie, Jermyn, Ian H., & Zerubia, Josiane. 2007. Higher-Order Active Contour Energies for Gap Closure. *J. Math. Imaging Vis.*, **29**(1), 1–20.

Schirmer, C. M., & Malek, A. M. 2007a. Prediction of complex flow patterns in intracranial atherosclerotic disease using computational fluid dynamics. *Neurosurgery*, **61**(4), 842–851.

Schirmer, C. M., & Malek, A. M. 2007b. Wall shear stress gradient analysis within an idealized stenosis using non-newtonian flow. *Neurosurgery*, **61**(4), 853–863.

Toyota, S., Iwaisako, K., Takimoto, H., & Yoshimine, T. 2008. Intravenous 3D digital subtraction angiography in the diagnosis of unruptured intracranial aneurysms. *American Journal of Neuroradiology*, **29**(1), 107–109.

Tsai, A., Yezzi, A., Jr., Wells, W., Tempany, C., Tucker, D., Fan, A., Grimson, W.E., & Willsky, A. Feb. 2003. A shape-based approach to the segmentation of medical imagery using level sets. *Medical Imaging, IEEE Transactions on*, **22**(2), 137–154.

Tyrrell, J.A., di Tomaso, E., Fuja, D., Tong, R., Kozak, K., Jain, R.K., & Roysam, B. 2007. Robust 3-D Modeling of Vasculature Imagery Using Superellipsoids. **26**(2), 223–237.

Wang, Y., & Staib, L. 1998. Boundary finding with correspondence using statistical shape models.

Wörz, S., & Rohr, K. 2007. Segmentation and Quantification of Human Vessels Using a 3-D Cylindrical Intensity Model. *IEEE Trans. on Image Processing*, **16**(8), 1994–2004.

Xiang, Yang, Chung, Albert C. S., & Ye, Jian. 2006. An active contour model for image segmentation based on elastic interaction. *Journal of Computational Physics,*, **219**(1), 455–476.

Xie, Xianghua, & Mirmehdi, Majid. 2008. MAC: Magnetostatic Active Contour Model. *IEEE Transactions on Pattern Analysis and Machine Intelligence*, **30**(4), 632–646, Accepted.